radiation

MDPI

Article

Reproducing the NIRS-QST Clinical Dose Calculations for Carbon Ion Radiotherapy Using Microdosimetric Probability Density Distributions

Alessio Parisi *, Keith M. Furutani, Shannon Hartzell and Chris J. Beltran

Department of Radiation Oncology, Mayo Clinic, Jacksonville, FL 32224, USA
* Correspondence: parisi.alessio@mayo.edu

Simple Summary: Carbon ion radiotherapy is an advanced cancer treatment that requires accurate calculations to account for the distinct biological effects of ions compared to the X-rays of conventional radiotherapy. In this work, we discuss an approach that uses experimentally measurable physical quantities to replicate established calculations used in clinical settings. By comparing our method with the current standard, we demonstrated that it produces results that are consistent within 2%. The proposed approach supports the advancement of treatment plans, ensures compatibility with the existing reference methodology, and provides a framework for improved quality assurance in ion radiotherapy.

Abstract: Ion radiotherapy requires accurate relative biological effectiveness (RBE) calculations to account for the markedly different biological effects of ions compared to photons. Microdosimetric RBE models rely on descriptions of the energy deposition at the microscopic scale, either through radial dose distributions (RDDs) or microdosimetric probability density distributions. While RDD approaches focus on the theoretical description of the energy deposition around the ion track, microdosimetric distributions offer the advantage of being experimentally measurable, which is crucial for quality assurance programs. As the results of microdosimetric RBE models depend on whether RDD or microdosimetric distributions are used, the model parameters are not interchangeable between these approaches. This study presents and validates a method to reproduce the published reference biological and clinical dose calculations at NIRS-QST for only carbon ion radiotherapy by using the modified microdosimetric kinetic model (MKM) alongside microdosimetric distributions instead of the reference RDD approach. To achieve this, Monte Carlo simulations were performed to estimate the variation of the radiation quality within and outside the field of pristine and spread-out Bragg peaks. By appropriately optimizing the modified MKM parameters for microdosimetric distributions assessed within water spheres, we successfully reproduced the results of calculations using the reference NIRS-QST RDD, generally within 2%.

Keywords: carbon ion radiotherapy; microdosimetry; modified MKM; Monte Carlo; PHITS; RBE

check for updates

Academic Editor: Salvatore Gallo

Received: 6 December 2024
Revised: 20 December 2024
Accepted: 21 December 2024
Published: 30 December 2024

Citation: Parisi, A.; Furutani, K.M.; Hartzell, S.; Beltran, C.J. Reproducing the NIRS-QST Clinical Dose Calculations for Carbon Ion Radiotherapy Using Microdosimetric Probability Density Distributions. *Radiation* **2025**, *5*, 2. https://doi.org/10.3390/radiation5010002

Copyright: © 2024 by the authors. Licensee MDPI, Basel, Switzerland. This article is an open access article distributed under the terms and conditions of the Creative Commons Attribution (CC BY) license (https://creativecommons.org/licenses/by/4.0/).

1. Introduction

Ion therapy is an advanced form of external cancer radiotherapy that uses accelerated ions to irradiate the target volumes. Protons and carbon ions are currently the most commonly used ions [1–3], while the utilization of helium, oxygen, and neon ions is being explored for single- or multi-ion treatments [4–6]. Due to the different nature of the energy

deposition between ions and the X-rays of conventional therapy, their biological effects differ [7–10]. This dissimilarity is considered during treatment planning through a scaling factor named the relative biological effectiveness (RBE). The RBE is defined as the ratio of the absorbed dose required with a reference radiation, typically photons, to that with ions to obtain the same biological effect [11]. In the case of protons, a fixed RBE value of 1.1 is generally employed in clinics [8,12,13]. Extensive discussion is ongoing regarding the need to consider the potential variations in the proton RBE at low energies [3,14–19]. In contrast, biological models are routinely employed during treatment planning in carbon ion radiotherapy to account for the marked RBE variations as a function of the biological system, endpoint, absorbed dose, particle type, and kinetic energy [20–28].

Three main RBE models are used in clinical practice with carbon ions: the first version of the local effect model (LEM I) [29], the mixed beam model (MBM) [30], and the modified microdosimetric kinetic model (modified MKM) [31]. The LEM and MBM, developed respectively at the Society for Heavy Ion Research (GSI) Helmholtz Centre for Heavy Ion Research in Germany and at the National Institute of Radiological Sciences within the National Institutes for Quantum Science and Technology (NIRS-QST) in Japan, are the first approaches used for the RBE calculations in carbon ion therapy. Although the LEM has undergone several updates over the years [32–34], its first version (LEM I) [29] remains the most commonly used in clinical practice. In 2011, NIRS-QST introduced pencil beam scanning delivery for carbon radiotherapy and replaced the semi-phenomenological MBM with the microdosimetry-based modified MKM [23,24].

In order to carry out RBE calculations using microdosimetric models [35,36], three components are needed: (I) a description of the energy deposition at the microscopic scale (microdosimetry), (II) a theoretical RBE model to correlate the microdosimetric physical information with the biological effects, and (III) model parameters specific to the chosen biological endpoint.

The microdosimetric quantities (I) needed to compute the RBE can be assessed through experimental measurements and computer simulations. Notably, the results markedly depend on the characteristics of the detector (e.g., material, size, and shape of the sensitive volume) and the simulation approach [37–41]. Therefore, even for a fixed biological system, biological endpoint, and RBE model, the optimized model parameters can vary considerably [42] and are not interchangeable between users employing different approaches to estimate the microdosimetric distributions [43,44].

The biological and clinical RBE-weighted dose system at NIRS-QST for carbon ion radiotherapy [23,24] relies on microdosimetric calculations based on the Kiefer–Chatterjee radial dose distribution (KC RDD) [45,46] for cylindrical water targets. Mayo Clinic Florida is currently installing the first-in-America proton-carbon ion radiotherapy center in Jacksonville, Florida [47]. The RBE calculations at Mayo Clinic Florida [42,48] will primarily be based on microdosimetric distributions computed for spherical water targets using an analytical microdosimetric function (AMF) [49,50].

In this work, we present a method to reproduce the modified MKM calculations at NIRS-QST using the spherical AMF instead of the cylindrical KC RDD. This article includes a systematic benchmark in several clinically relevant scenarios, both in field and out of field.

2. Methodology

2.1. Linear Quadratic Model, RBE, and Clinical Dose

Following the dose–prescription system used at NIRS-QST, the clonogenic survival of human salivary gland tumor cells (HSG cell line) was considered the relevant biological

endpoint for the RBE calculations [20,23,24]. The linear quadratic model (LQM) [51,52] was used to describe the cell surviving fraction (S) as a function of the absorbed dose (D):

$$S = exp\left(-\alpha D - \beta D^2\right) \quad (1)$$

where α and β are exposure- and cell-specific fitting parameters.

The RBE as a function of the absorbed dose D of the radiation under investigation (RBE_D) was calculated as [18]:

$$RBE_D = \frac{\sqrt{\alpha_{ref}^2 + 4\beta_{ref}(\alpha D + \beta D^2)} - \alpha_{ref}}{2\beta_{ref} D} \quad (2)$$

where α, β, α_{ref}, and β_{ref} are LQM terms for the radiation under investigation and the reference radiation, respectively.

The clinical dose was estimated as the product between the absorbed dose, the dose-dependent RBE for the HSG cell line, and a fixed clinical scaling factor of 2.41 [24]:

$$D_{clinical} = 2.41\ D_{absorbed}\ RBE_{D,HSG\ cell\ line} \quad (3)$$

The radiation quality at the center of the NIRS-QST carbon ion spread-out Bragg peak (SOBP) with a 60 mm width and a maximum energy of 350 MeV/n (energy per nucleon) was used as the reference radiation for the computation of the RBE_D (α_{ref} = 0.764 Gy^{-1}, β_{ref} = 0.0615 Gy^{-2}) [24]. The LQM terms α and β were estimated using the modified MKM, as described in the Section 2.2.

2.2. Modified MKM

The modified MKM [31] is a RBE model derived from the theoretical framework of the MKM [53], which is itself rooted in the theory of dual radiation action [54,55]. The original MKM and its subsequent versions [31,42,53,56,57] were developed to describe and predict the heightened RBE of ions when compared to photons. To this end, these models postulate the existence of subnuclear radiation structures, referred to as domains, where the accumulation of both lethal and sublethal radiation damage leads to the eventual loss of the cell's clonogenic capability.

The variations in the microscopic pattern of the energy deposition within these domains is described by microdosimetric quantities, such as the specific energy and the lineal energy. The single-event specific energy z is defined as the ratio ε/m between the energy imparted by a single event ε in a domain and the mass m of that domain [58,59]. Similarly, the lineal energy y represents the ratio $\varepsilon/\bar{l}$ between the energy imparted by a single event ε in a domain and the mean chord length $\bar{l}$ of that domain [58,59]. In a second step, these microdosimetric quantities are used to estimate the cell survival and thus the RBE.

According to the modified MKM [31], the quadratic term of the LQM is considered radiation-independent and equal to that after irradiation with photons ($\beta = \beta_0 = \beta_{ref}$ = 0.0615 Gy^{-2} for the HSG cell line). In contrast, α depends on the radiation quality and can be estimated as [31]:

$$\alpha = \alpha_0 + \beta_0 \bar{z}_D^* \quad (4)$$

where α_0 represents the initial slope of the survival curve for very sparsely ionizing radiation, β_0 is the radiation-independent quadratic term of the LQM, and $\bar{z}_D^*$ is the saturation-corrected dose-mean specific energy, which accounts for the overkill effects for densely ionizing radiation. The computation of $\bar{z}_D^*$ depends on the approach used for assessing the microdosimetric distributions (i.e., KC RDD or AMF), as detailed below.

2.3. Calculation of $\bar{z}_D^*$ with the KC RDD

In line with the methodology employed at NIRS-QST [23], we estimated $\bar{z}_D^*$ as a function of the kinetic energy (0.1–1000 MeV/n) for ^{1}H, ^{4}He, ^{7}Li, ^{9}Be, ^{11}B, ^{12}C, and ^{20}Ne ions. The first six ions (Z = 1–6) were considered as they are required for the RBE calculations in carbon ion therapy [23]. Neon ions were also included as they were previously used to determine the model parameters for the modified MKM at NIST-QST [23].

These track segment calculations, disregarding the particle slowing down within the microscopic volume and nuclear reactions, were carried out with a validated in-house implementation of the KC RDD [44]. According to the KC RDD, the dose distribution at a distance R around the track of a given ion is constant within a zone proximal to the ion track, named the core. Outside the core, the radial dose due to secondary electrons in the penumbra region is proportional to $1/R^2$. For a given ion, the radial dose distribution was computed knowing the ion energy, mass, effective charge, velocity relative to light, and the unrestricted linear energy transfer (LET) in water, as detailed in previous works [23,60]. The unrestricted LET in water was estimated using the ATIMA stopping power model implemented in the Monte Carlo Particle and Heavy Ion Transport code System (PHITS) version 3.32 [49].

In a second step, we assessed the specific energy $z(x)$ within a cylindrical water target (radius r_{d} = 0.32 µm, height = 0.64 µm [23]) as a function of the distance between the axes of the cylinder and the ion's track. This distance is commonly referred to as the impact parameter x.

Thirdly, the specific energy as a function of the impact parameter was corrected for the onset of overkill effects for densely ionizing radiation [23]. The saturation-corrected specific energy z_{sat} was therefore computed as [23]:

$$z_{sat}(x) = \frac{z_0^2}{z(x)}\left(1 - e^{-\frac{z(x)^2}{z_0^2}}\right) \tag{5}$$

where $z(x)$ is the specific energy as a function of the impact parameter x, and z_0 (Equation (6) [23]) is a saturation coefficient dependent on the radiation-independent quadratic term of the LQM (β_0), the radius of the subnuclear domains (r_d), and the radius of the cell nucleus (R_n).

$$z_0 = \frac{\left(\frac{R_n}{r_d}\right)^2}{\sqrt{\beta_0\left[1 + \left(\frac{R_n}{r_d}\right)^2\right]}} \tag{6}$$

Finally, the dose-mean specific energy $\bar{z}_D^*$ was calculated as [23]:

$$\bar{z}_D^* = \frac{\int_0^{R_p + r_d} z_{sat}(x) z(x) 2\pi x \, dx}{\int_0^{R_p + r_d} z(x) 2\pi x \, dx} \tag{7}$$

where $z_{sat}(x)$ is the saturation-corrected specific energy, $z(x)$ is the specific energy, x is the impact parameter, R_p is the radial extension of the penumbra according to the KC RDD, and r_d is the radius of the subnuclear domains.

The model parameters for human salivary tumor cells (HSG cell line), the reference cell line for RBE calculations with the modified MKM at NIRS-QST, were extracted from the literature [23,24] and are listed in Table 1.

Table 1. Overview of the modified MKM parameters for clinical dose calculations with the KC RDD and the AMF. * parameters from NIRS-QST [23,24]. ** parameters determined in this study to best reproduce the KC RDD calculations.

Approach Used for the Computation of the Microdosimetric Distributions	α_0 [Gy^{-1}]	α_{ref} [Gy^{-1}]	β_0=β_{ref} [Gy^{-2}]	r_d [µm]	R_n [µm]
KC RDD	0.172 *	0.764 *	0.0615 *	0.32 *	3.9 *
AMF	0.085 **	0.764 *	0.0615 *	0.333 **	4.28 **

2.4. Calculation of $\bar{z}_D^*$ with the AMF

The AMF [61,62] is an analytical approach that can instantaneously compute the microdosimetric probability density distributions given the particle type, its energy, and a microdosimetric target size as input. In the AMF, the targets used for the assessment of the microdosimetric distributions are liquid water spheres with a user-defined radius between 1.5 nm and 1 µm.

The original version of the AMF, published in 2006 [61], was developed to enable the macroscopic Monte Carlo code PHITS [49] to efficiently perform microdosimetric calculations over macroscopic bodies. At first, the microdosimetric distributions were computed for different ions, energies, and spherical targets of different sizes. These calculations were based on a hybrid approach combining Chatterjee's description of the energy deposition in the core region [45] (as in the KC RDD in Section 2.2), the production cross-sections of secondary electrons (delta-rays) based on the model by Butts and Katz [63], and detailed track structure simulations of the energy depositions of such secondary electrons with the Monte Carlo code TRACEL [64]. Based on the work of Olko and Booz [65], an analytical approach was developed to reproduce the microdosimetric simulations [61].

The original AMF was found to satisfactorily reproduce the spectra measured with gas detectors irradiated with protons [66,67], helium ions [66,68], carbon ions [61,68], silicon ions [66], and neutrons [69]. Furthermore, the AMF [61] was instrumental in the development of microdosimetric models of radiation action, such as the stochastic MKM [57], the Microdosimetric d(z) Model [70], the integrated MKM [71], the V79 biological weighting function [72], and the Mayo Clinic Florida MKM [42]. These models were utilized to successfully describe and predict the response of cell lines [36,42,57,67,72–78], thermoluminescent detectors [70,79–83], and optically stimulated luminescent detectors [84,85] exposed to various types of radiation. Nonetheless, limitations in the AMF results were reported in the case of low-energy (<10 MeV/n) heavy ions [36].

An updated version of the AMF was presented in 2023 [62]. The newer AMF was developed by fitting the results of detailed simulations with the track structure modes of the Monte Carlo code PHITS [49] for electrons, ^{1}H, ^{4}He, ^{12}C, ^{20}Ne, ^{28}Si, and ^{56}Fe ions. Unlike the original AMF [61], the newer AMF [62] also allows the computation of the number of ionizations, generally referred to as the ionization cluster size distribution. Furthermore, while the original AMF [61] relied on Chatterjee's simplified description of the energy deposition in the ion core region [45], the newer AMF employed a track structure approach to estimate the direct energy depositions from the primary ions [62]. A comparative analysis of the two AMFs indicates that the newer version more accurately reproduces the microdosimetric distributions measured with gas detectors [62] and the results of in vitro RBE experiments [50].

In this work, we used the newer AMF [62] to estimate the dose probability distribution of the lineal energy $d(y)$ in track segment conditions. The use of the lineal energy distributions instead of specific energy distributions arises from their more limited dependence on the microdosimetric target size and shape, making the lineal energy the preferred mi-

crodosimetric quantity when comparing distributions assessed with various approaches or different detectors [37,40,41]. In a second step, we computed the saturation-corrected dose-mean specific energy $\bar{z}_D^*$ as [31]:

$$\bar{z}_D^* = \frac{y_0^2}{\rho \pi r_d^2} \int_0^{+\infty} \frac{\left[1 - \exp\left(-y^2/y_0^2\right)\right]}{y} d(y) dy \quad (8)$$

where ρ is the density of a domain, r_d is the radius of the domain, $d(y)$ is the dose distribution of the lineal energy y, and y_0 is a saturation parameter (Equation (9) [31]) dependent on the radiation-independent quadratic term of the LQM (β_0), the radius of the subnuclear domains (r_d), and the radius of the cell nucleus (R_n).

$$y_0 = \frac{\rho \pi r_d R_n^2}{\sqrt{\beta_0 \left(r_d^2 + R_n^2\right)}} \quad (9)$$

The numerical values of r_d and R_n were estimated to best reproduce the results of the KC RDD, as described in the Section 2.5, and are listed in Table 1.

2.5. Determination of the Modified MKM Parameters for the AMF

At first, following the published methodology [18,50], we assessed the dose probability distribution of the lineal energy $d(y)$ for ^{1}H, ^{4}He, ^{7}Li, ^{9}Be, ^{11}B, ^{12}C, and ^{20}Ne ions with kinetic energy ranging from 0.1 to 1000 MeV/n. The target used in the microdosimetric simulations was liquid water spheres with a radius equal to 0.30 μm radius. Subsequently, we optimized the model parameters r_d, R_n, and α_0 of the modified MKM to best reproduce the α values computed using the KC RDD (Section 2.3) for clinically relevant carbon ions with LET up to 500 keV/μm. This was achieved by minimizing the relative deviation between the results of the AMF and the KC RDD. Although the radius of the subnuclear domains used in the modified MKM calculations was varied to best reproduce the NIRS-QST data, the microdosimetric simulations with PHITS were carried out only in the case of a 0.30 μm radius. This approach was adopted because, within the range of cell-specific domain radii employed in the MKM calculations, the lineal energy distributions are largely unaffected by the choice of radius in the computer simulations [50,77,86].

2.6. Benchmark

To benchmark our proposed approach, we compared the AMF results with the corresponding KC RDD calculations in several scenarios.

At first, using the model parameters for the AMF determined in Section 2.5 to best reproduce the KC RDD calculations for ^{12}C ions, we calculated $\bar{z}_D^*$ and α as a function of the unrestricted LET for ^{1}H, ^{4}He, ^{7}Li, ^{9}Be, ^{11}B, and ^{20}Ne ions with energy between 0.1 and 1000 MeV/n. The obtained results were compared to the corresponding data computed with the KC RDD.

Secondly, we estimated $D_{10\%}$ for the HSG cell line as a function of the unrestricted LET for ^{4}He, ^{12}C, and ^{20}Ne ions using Equation (10) [24]:

$$D_{10\%} = \frac{-\alpha + \sqrt{\alpha^2 - 4\,\beta \ln(0.1)}}{2\,\beta} \quad (10)$$

where α and β are the LQM terms after ion exposure.

The AMF-based $D_{10\%}$ values for the HSG cell line were then compared with the corresponding results using the KC RDD and in vitro data [87].

Finally, we compared the results of the modified MKM calculations using the AMF and the KC RDD within a water phantom for two pristine carbon ion beams (100 and

430 MeV/n) and a SOBP resembling the one used at NIRS-QST for the definition of the reference radiation (SOBP with a flat clinical dose profile of 5.8 GyRBE between 15 and 21 cm [24]).

2.7. Monte Carlo Simulations Within a Water Phantom

The simulations were performed using the Monte Carlo code PHITS version 3.32 [49] on the mForge cluster of the National Center for Supercomputing Applications (NCSA, Urbana, IL, USA). The calculations were parallelized across 1152 hyperthreaded Intel Xeon cores operating at 2.6 GHz.

The Electron Gamma Shower version 5 (EGS5) [88] was used to simulate the transport of photons, electrons and positrons. The macroscopic energy loss of the other charged particles was estimated using the PHITS-implemented stopping power model ATIMA (https://web-docs.gsi.de/~weick/atima/, accessed on 26 December 2024). The energy and angular straggling, deactivated by default, were modeled with the Landau Vavilov formula [89] and with Lynch's diffusion formula [90], respectively. The recommended nuclear models [49] were used in the PHITS calculations, namely the Japan Atomic Energy Research Institute (JAERI) Quantum Molecular Dynamics (JQMD) [91], the Intranuclear Cascade Model of Liege (INCL) [92], and the Generalized Evaporation Model (GEM) [93]. The transport and interaction of low-energy neutrons were modeled with the Event Generator mode version 2 [94,95]. Consistent with the KC RRD-based modified MKM tables [23], the transport cutoff of all the ions was set to 0.1 MeV/n. The transport cutoff of the neutrons was 10^{-11} MeV, while all the other particles (e.g., photons, electrons, positrons, pions, kaons, muons…) were transported down to 1 keV. As recommended in Report 90 of the International Commission on Radiation Units and Measurements (ICRU) [96], the mean excitation energy of water was set to 78 eV. As required for the use of the AMF, the delta-rays placed in motion by the ions were not transported to avoid double counting their contribution to the microdosimetric distributions (PHITS manual, https://phits.jaea.go.jp/manual/manualE-phits.pdf, accessed on 26 December 2024).

A simulated liquid water phantom with dimensions of $100 \times 100 \times 350$ mm^3 was irradiated with carbon ion beams orthogonally incident on the center of one of the square surfaces. Two monoenergetic beams were modeled, representing the lowest and highest energy layers of the upcoming carbon ion therapy center at Mayo Clinic Florida: 100 MeV/n and 430 MeV/n, respectively. The initial energy spread was set to 1.5% for the 100 MeV/n beam and 0.2% for the 430 MeV/n beam. The ion beams had a Gaussian spatial spread of 2 mm for the 100 MeV/n beam and 1 mm for the 430 MeV/n beam.

Additionally, an iteratively determined [97] poly-energetic energy spectrum was employed to generate an SOBP with a flat clinical dose profile of 5.8 GyRBE between depths of 150 and 210 mm. This SOBP was designed to resemble the one used at NIRS-QST for the definition of the reference radiation quality [24]. The initial diameter of the circular SOBP beam was 60 mm.

In line with the approach of previous works [18,41,78,97], we used three different scorers, referred to as tallies in PHITS, to estimate the absorbed dose (T-Deposit tally), the unrestricted LET distributions (T-LET tally, based on the ATIMA stopping power model), and the lineal energy distributions (T-SED tally, based on the newer AMF) at multiple locations within the water phantom.

10^7 and 10^8 primary carbon ions were simulated for the pristine beams and the SOBP, respectively. The total running time was approximately 4 h (100 MeV/n pristine), 14 h (430 MeV/n pristine), and 12 h (SOBP). The dissimilar number of simulated histories between the pristine beams and the SOBP was chosen to ensure a comparable amount of primary ions crossing the scoring volumes used for the assessment of the physical

quantities as a function of the depth in water within the phantom. Here, the pristine beams (initial spot size of 1–2 mm) were totally encompassed by the scoring volumes, while approximately 1/9 of the SOBP beam was covered by the scoring volumes. More details are given in the following sections. The statistical error associated with the assessment of α as a function of the depth in water was less than 0.5% at all the locations, including the fragmentation tail.

2.7.1. Quantities as a Function of the Depth in Water

To assess the depth dependence of the dose, LET, and lineal energy, these quantities were scored across 350 cylindrical volumes, each with a height of 1 mm, placed sequentially along the ion beam path within the water phantom. For the pristine beams, characterized by a small initial spot size (2 and 1 mm for the 100 and the 430 MeV/n beam, respectively), the quantities were laterally integrated over cylindrical volumes with a radius of 50 mm. For the SOBP beam, which had an initial radius of 30 mm, the quantities were evaluated in the radially central part of the beam, using cylindrical volumes with a radius of 10 mm.

At each depth in water, the lineal energy distribution was computed by PHITS as the dose-weighted sum of the AMF-based lineal energy distributions of particles depositing energy within the chosen scoring volume. The obtained microdosimetric distributions represent the energy depositions that would be experienced by microscopic spherical targets (radius = 0.3 µm) scattered over the macroscopic computational cylinders placed at different depths in water within the phantom. Consistently with the RBE calculations at NIRS-QST [23], only the contributions of ions from H to C were included in the computation of the lineal energy distributions. At each depth in water, the obtained lineal distribution was processed to compute the α for the HSG cell line, as described in Sections 2.2 and 2.4. The lineal energy distributions were scored using a logarithmic binning from 0.01 to 100,000 keV/µm, with 50 bins per decade, for a total of 350 bins. The use of 50 bins per decade is a typical choice for binning microdosimetric distributions [59].

The computation of α with the KC RDD relied on pre-calculated α tables as a function of the unrestricted LET of H, He, Li, Be, B, and C ions (Section 2.3). At each depth within the phantom, the frequency distribution of the track-averaged unrestricted LET in water was separately assessed for each ion type between H and C. Each of these distributions was scored using a logarithmic binning from 0.1 to 1000 keV/µm with 500 bins per decade, for a total of 2000 bins. The more refined binning was necessary due to the deterministic nature of the LET and the associated smaller variance with respect to the lineal energy.

Afterwards, these LET distributions were processed to compute α as in Equation (11):

$$\alpha = \frac{\sum_{Z=1}^{6}\left[\sum_{i=1}^{2000}\alpha_i\left(\overline{LET}_i, Z\right)\cdot n\left(\overline{LET}_i, Z\right)\cdot\overline{LET}_i\cdot\Delta LET_i\right]}{\sum_{Z=1}^{6}\left[\sum_{i=1}^{2000} n\left(\overline{LET}_i, Z\right)\cdot\overline{LET}_i\cdot\Delta LET_i\right]} \quad (11)$$

where $\overline{LET}_i$ is the mean LET in the bin i, ΔLET_i is width of the bin i, $\alpha_i\left(\overline{LET}_i,\ Z\right)$ is the α value corresponding to the $\overline{LET}_i$ for the ion with atomic number Z, and $n\left(\overline{LET}_i,\ Z\right)$ is the number of counts (i.e., the frequency distribution of events) in the bin i.

2.7.2. Quantities as a Function of the Radial Distance from the Beam Axis

Secondly, as in a previous study [97], we assessed the radial variation of the dose, α, and RBE at different depths in water within the water phantom. This was achieved by evaluating the aforementioned quantities over non-overlapping cylindrical shells with 1 mm height and incremental inner and outer radii in 1 mm steps from 0 to 50 mm (i.e., 0–1 mm, 1–2 mm, . . ., 49–50 mm). The lineal energy distributions were calculated for microscopic spheres (radius = 0.3 µm) scattered over those macroscopic cylindrical

shells. The processing of the LET and lineal energy distributions follows the approach in Section 2.7.1.

In the case of the pristine 100 and 430 MeV/n beams, the radial variation of the investigated quantities was studied for four depths in water corresponding to the entrance channel (0–1 mm), the Bragg peak region characterized by a sharp increase in the absorbed dose (20–21 mm for the 100 MeV/n beam and 290–291 mm for the 430 MeV/n), the Bragg peak maximum (25–26 mm for the 100 MeV/n beam and 307–308 mm for the 430 MeV/n), and the fragmentation tail (28–29 mm for the 100 MeV/n beam and 330–331 mm for the 430 MeV/n). For the SOBP with a flat clinical dose profile between 150 and 210 mm, the chosen depths in water represent the entrance channel (0–1 mm), the middle of the SOBP (180–181 mm), the depth in the distal edge with the highest RBE (210–211 mm), and the fragmentation tail (230–231 mm).

3. Results

Figure 1 shows the linear term of the LQM (α) for the HSG cell line plotted as a function of the LET of carbon ions. Three in silico data series are compared, representing the results of the modified MKM combined with track segment calculations based on the KC RDD (NIRS-QST model parameters [23]) and the AMF (NIRS-QST model parameters and optimized model parameters). The model parameters for the calculations with the KC RDD were previously optimized at NIRS-QST by fitting the results of in vitro experiments with the HSG cell line [23]. It is evident that, if such parameters are employed with the AMF, the obtained α values differ significantly from those obtained with the KC RDD, with deviations of up to ~30%. These deviations arise from differences in the approach used for computing the microdosimetric quantities, as detailed in Sections 2.3 and 2.4. It was possible to compensate for these deviations by tuning the modified MKM parameters when used in conjunction with the AMF. These optimized model parameters for the AMF, as listed in Table 1, allowed to reproduce the KC RDD track segment calculations of α for carbon ions within 2% over the clinically relevant LET range of 9–550 keV/µm.

Figure 2 extends the comparison of the α values computed with the KC RDD (NIRS-QST model parameters) and the AMF (optimized model parameters) to ions other than carbon, namely ^{1}H, ^{4}He, ^{7}Li, ^{9}Be, ^{11}B, and ^{20}Ne. The horizontal and vertical axes remain unchanged across the panels to highlight the relative changes in α between the ion types. For ^{1}H and ^{4}He ions with LET < 3 keV/µm, the AMF predicts α values up to ~30% lower than those from the KC RDD. At higher LET, the agreement improves, with deviations within ~6%. In contrast, the AMF-based calculations were found to overestimate the KC RDD results for energetic ^{7}Li, ^{9}Be and ^{11}B ions (LET < 10 keV/µm) by up to 29%, 18%, and 7%, respectively. For LET > 6 keV/µm, the α values from both approaches agree within ~10%. In the case of ^{20}Ne ions, the results of the AMF and the KC RDD are very similar (within 2%) up to LET values of 300 keV/µm. At higher LET, the AMF results are up to 17% lower than the corresponding KC RDD calculations.

As in the reference NIRS-QST work [23], Figure 3 compares the dose required to achieve a 10% surviving fraction ($D_{10\%}$) for the HSG cell line as computed using the modified MKM with the corresponding in vitro data [87] for helium, carbon, and neon ions between 10 and 1000 keV/µm. For LET values below 200 keV/µm, the $D_{10\%}$ decreases with the increase in the LET, reflecting the enhanced efficiency in inducing lethal damage to the cells. For a given LET within this range, the $D_{10\%}$ is lower as the ion's atomic number decreases. This effect arises from differences in the track structure of ions with the same LET. Heavier ions, possessing greater kinetic energy, release secondary electrons with longer ranges, leading to a radially less dense pattern of energy deposition. At higher LET values, the trend reverses due to the onset of overkill effects.

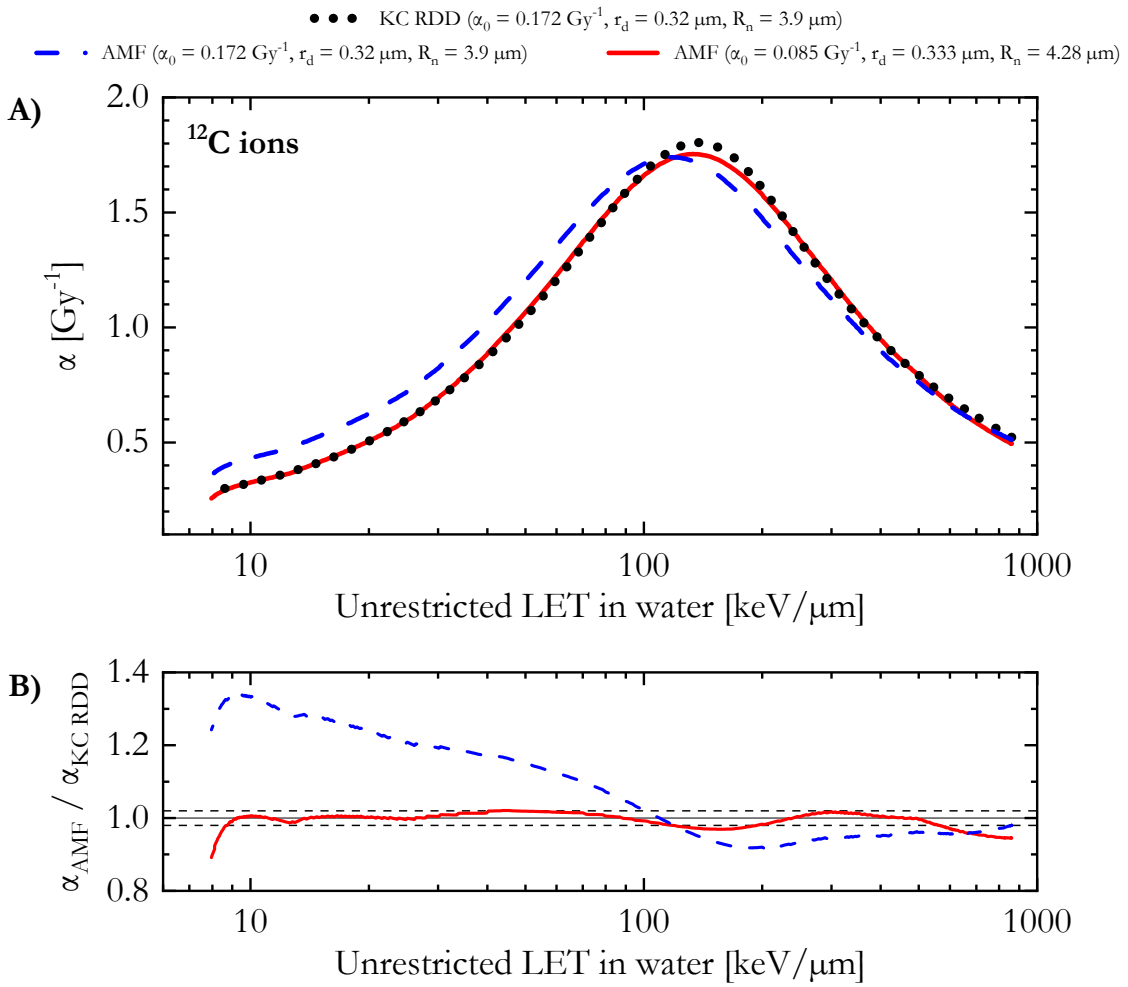


Figure 1. (**A**) Comparison of the α values for the HSG cell line calculated using the modified MKM in conjunction with track segment calculations based on the KC RDD (NIRS-QST model parameters) and the AMF (NIRS-QST model parameters and optimized model parameters to reproduce the KC RDD results) in the case of ^{12}C ions. (**B**) The ratio of the α values computed using the KC RDD and the AMF. The horizontal dashed lines indicate a deviation of ±2%.

The AMF-based calculations reproduced the KC RDD results up to 600 keV/μm, generally within 2%, with deviations up to 5% for low-energy helium ions (LET > 70 keV/μm). Larger deviations were observed for neon ions with LET > 600 keV/μm, where the $D_{10\%}$ values computed using the AMF overestimated the KC RDD calculations by up to 10%. Nonetheless, this overestimation seems to bring the AMF results closer to the corresponding in vitro data.

Panels A of Figures 4 and 5 show the α values for the HSG cell line computed with the modified MKM as a function of the depth in water for the 100 and 430 MeV/n beams. These beams have initial spot sizes of 2 and 1 mm, respectively, and the results were radially integrated from 0 to 50 mm around the beam axis. The AMF- and KC RDD- based calculations agreed within 2%, except in the fragmentation tail of the 100 MeV/n beam, where the AMF overestimated the KC RDD by up to 4.5%. The agreement between these two approaches is further examined in panels B–D of Figures 4 and 5 as a function of the radial distance from the beam axis at the four depths in water indicated by the black open squares in panels A. Due to the steep decrease in the absorbed dose with the radial distance, voxels located farther from the beam axis may receive doses that are not clinically relevant. The vertical blue dashed lines in panels B–D of Figures 4 and 5 mark the radial distances beyond which voxels receive less than 1% of the absorbed dose at the Bragg peak maximum.

For all the voxels within these radial distances, the AMF and KC RDD calculations agree within 2%. At larger distances, the AMF-based calculations were found to underestimate the KC RDD results by up to approximately 7% and 13% for the 100 and the 430 MeV/n beams, respectively.

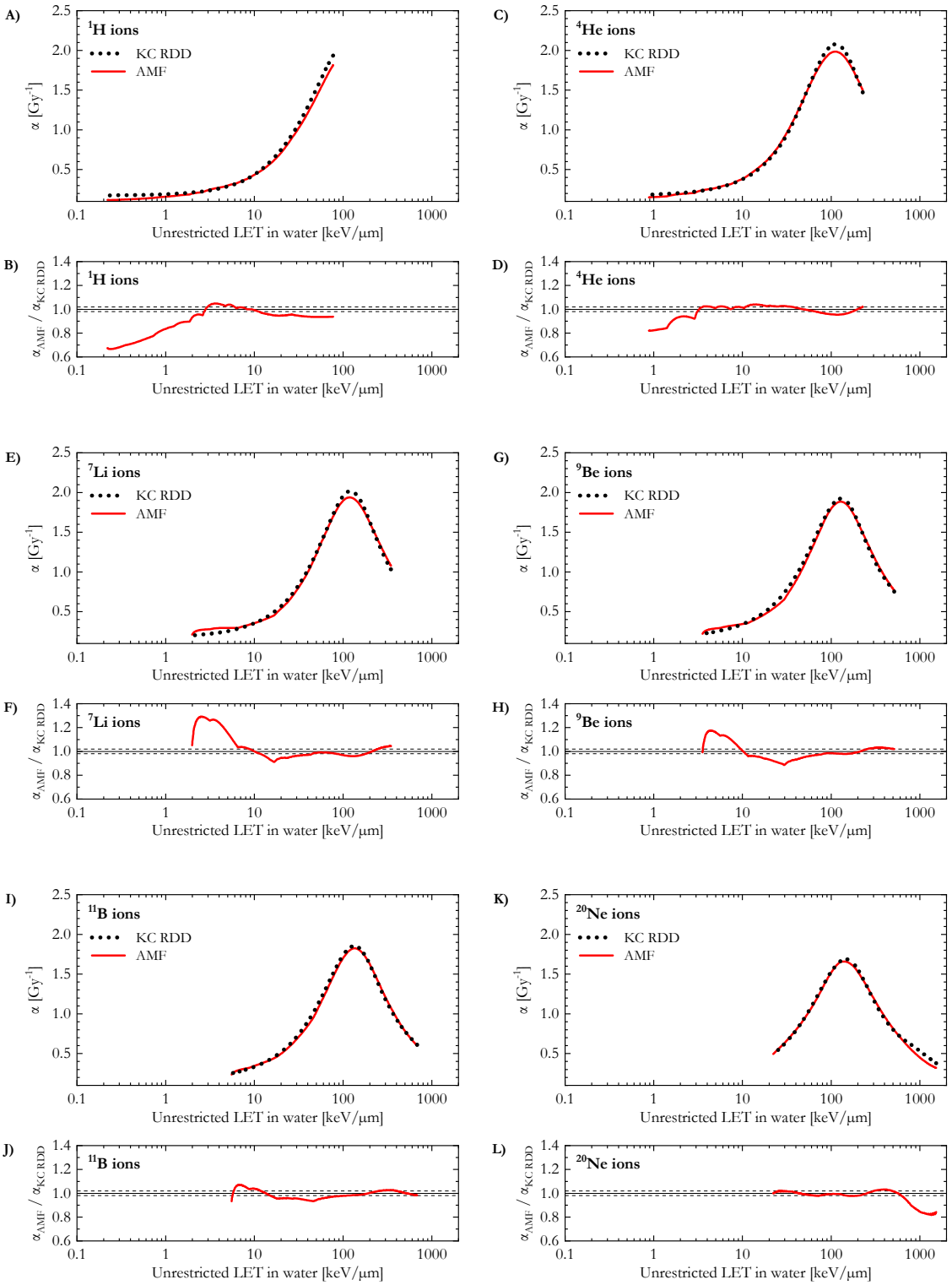


Figure 2. Comparison of the α values for the HSG cell line calculated using the modified MKM in conjunction with track segment calculations based on the KC RDD (NIRS-QST model parameters) and the AMF (optimized model parameters) in the case of ^{1}H, ^{4}He, ^{7}Li, ^{9}Be, ^{11}B, and ^{20}Ne ions. The horizontal dashed lines plots indicate a deviation of ±2%.

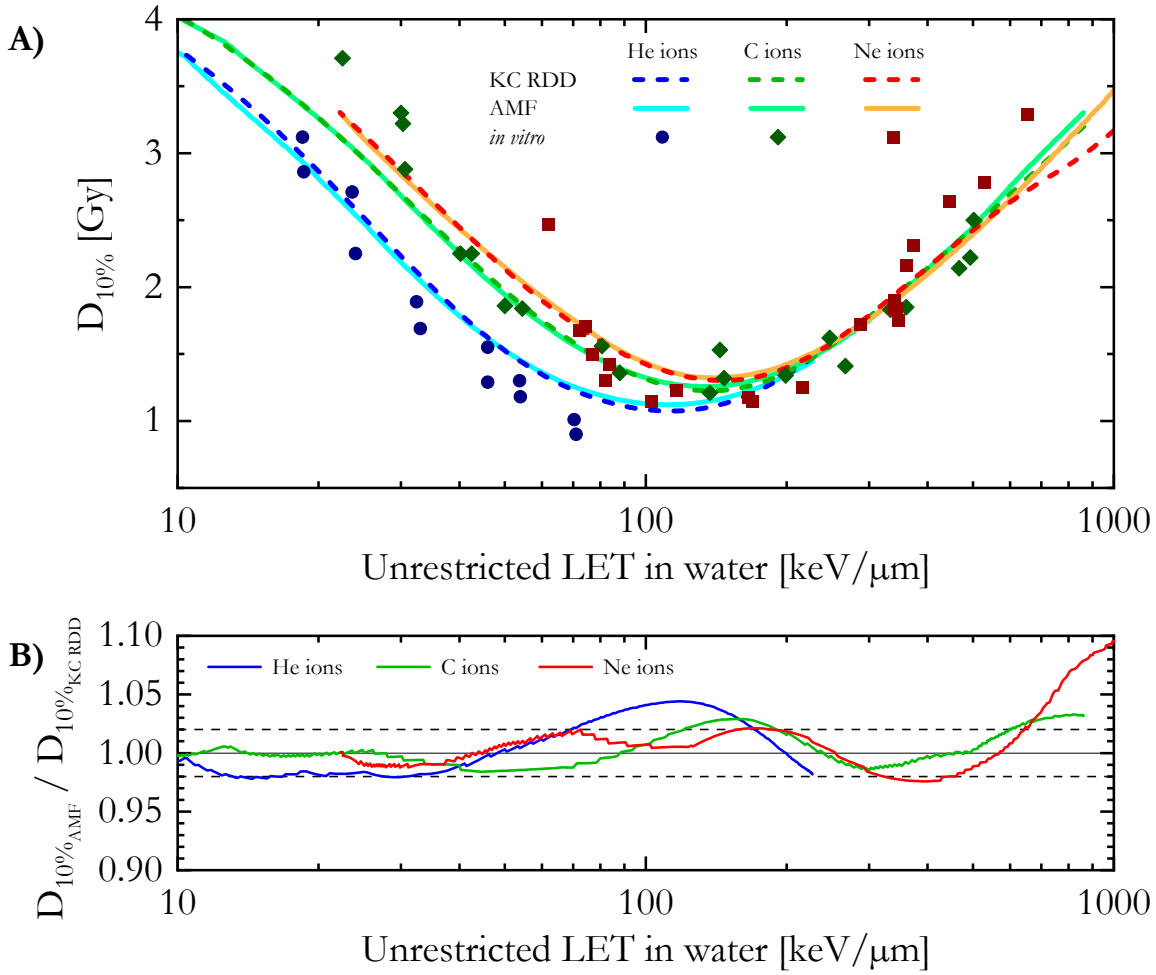


Figure 3. (**A**) The absorbed dose required to achieve a 10% surviving fraction ($D_{10\%}$) for the HSG cell line exposed to helium, carbon, and neon ions: comparison between calculations using the modified MKM in conjunction with the KC RDD (NIRS-QST model parameters) and the AMF (optimized model parameters), and in vitro data (reported as a function of the dose-mean unrestricted LET). (**B**) The ratio of the $D_{10\%}$ between the modified MKM calculations based on the AMF and the KC RDD.

The α values for the HSG cell line and the clinical dose in the radially central part of the carbon ion SOBP (i.e., radially integrated between 0 and 10 mm) are plotted in Figure 6A as a function of the depth in water within the phantom. For both quantities, the AMF-based results aligned with the KC RDD calculations within 2%. The agreement was generally better for the clinical dose, as this quantity is a function of α (varying between the AMF or the KC RDD) and β, which remains constant in the modified MKM calculations. Similarly, the AMF and KC RDD calculations yielded similar results in describing the radial variation of α and the clinical dose within the field (0–30 mm) and its near penumbra (30–35 mm), with deviations reaching up to 10% in low-dose regions farther from the beam axis. Interestingly, the clinical dose within certain voxels located in the penumbra of the SOBP is lower than the absorbed dose. This occurs because the secondary fragments in this region exhibit a sparser pattern of energy deposition (i.e., lower LET) compared to the reference radiation, namely the quality in the center of the carbon SOBP. Consequently, the RBE relative to this reference radiation can be significantly lower than 1. This phenomenon can also be explained by comparing the radially dependent α values in Figure 6 with the reference value listed in Table 1 (α_{ref} = 0.764 Gy^{-1}).

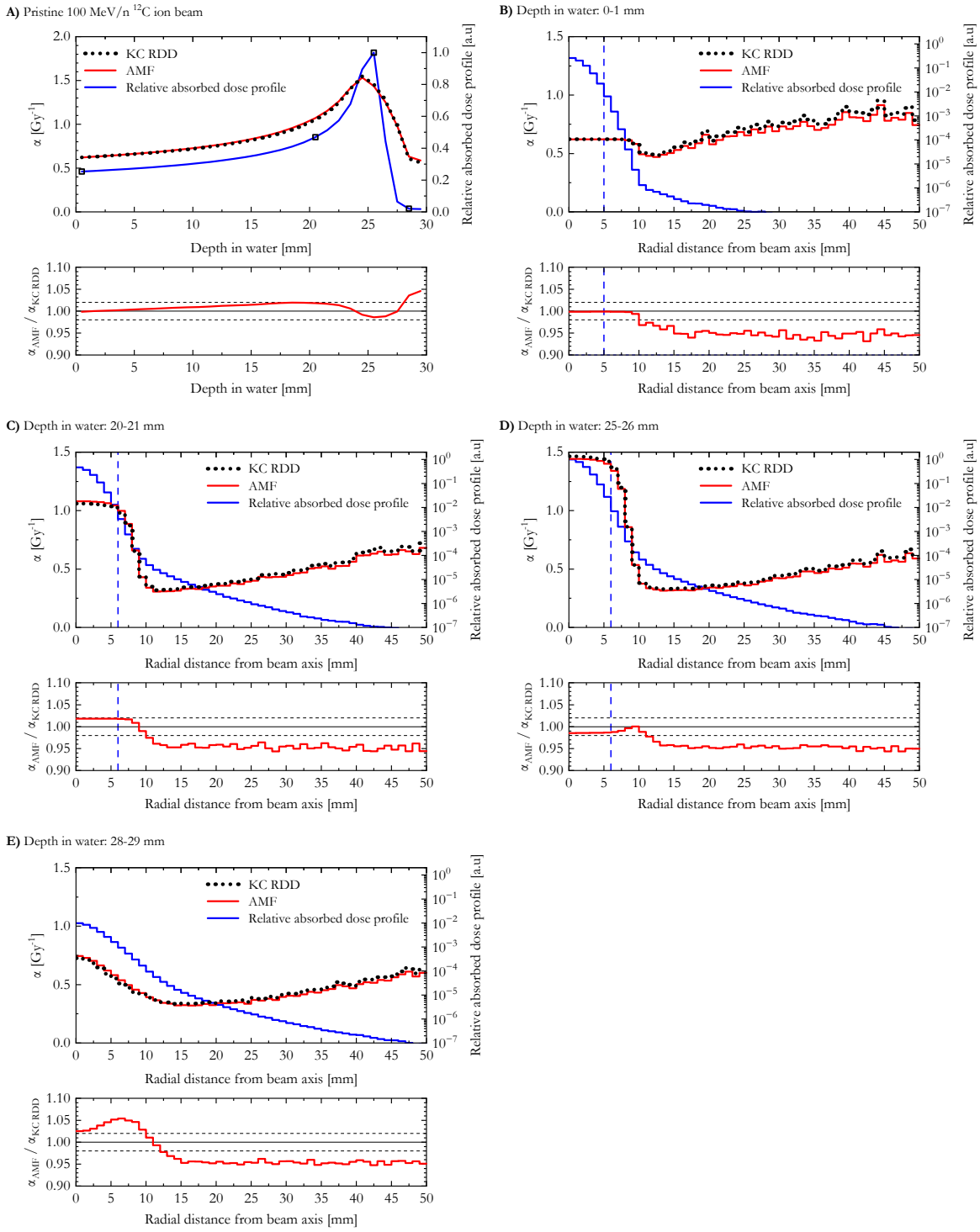


Figure 4. (**A**) α for the HSG cell line as a function of the depth in water along the Bragg peak for a single spot (σ_{xy} = 2 mm) of a 100 MeV/n carbon ion beam. The results of the modified MKM calculations based on the KC RDD (NIRS-QST model parameters) and the AMF (optimized model parameters) were radially integrated between 0 and 50 mm around the axis of the beam. (**B**–**E**) Comparison between the calculations using the modified MKM in conjunction with the KC RDD (NIRS-QST model parameters) and the AMF (optimized model parameters) as a function of the radial distance from the beam axis at four depths in water along the pristine peak (indicated by the black open squares in panel (**A**)). The vertical blue dashed lines demarcate voxels receiving at least 1% of the absorbed dose at the Bragg peak maximum.

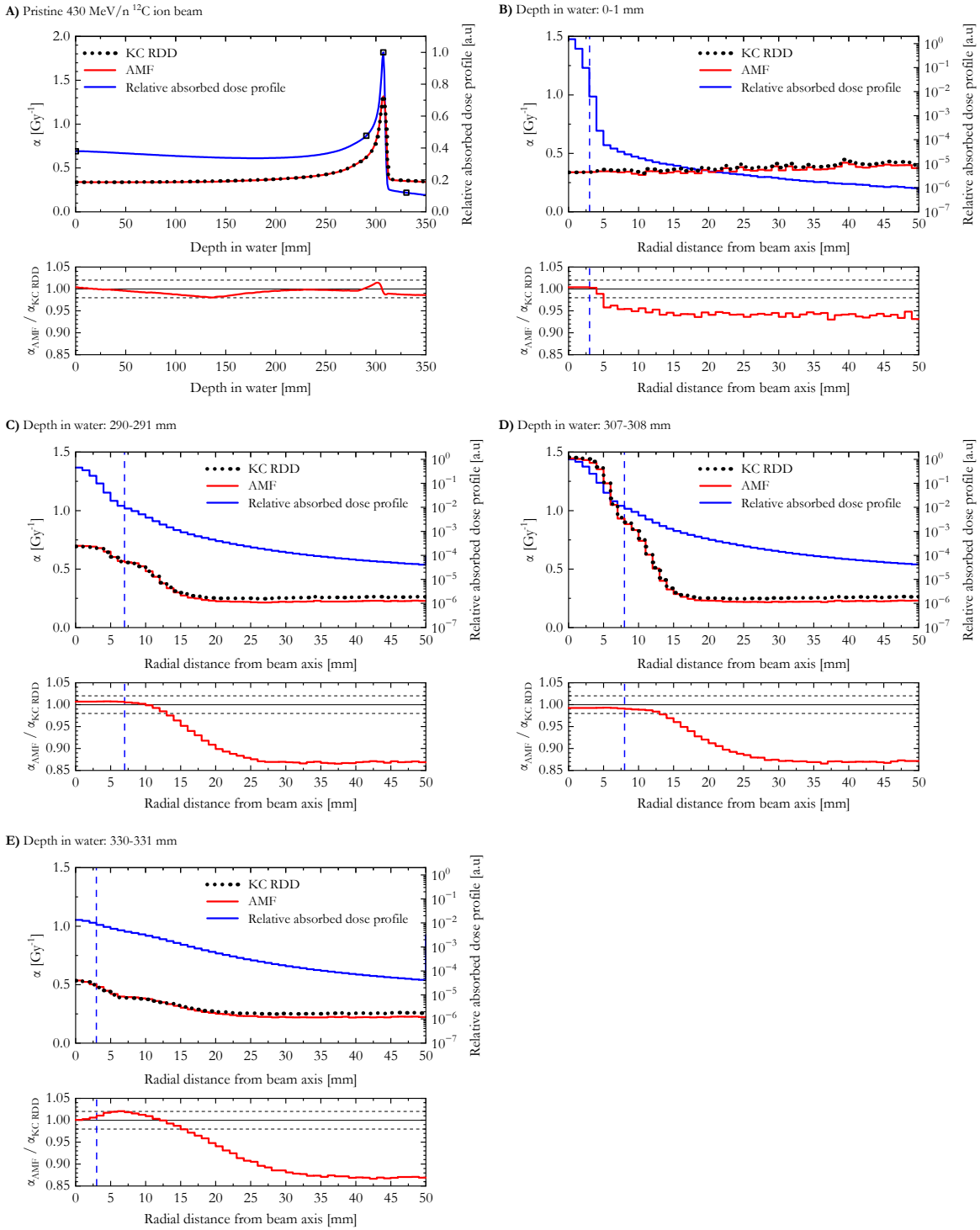


Figure 5. (**A**) α for the HSG cell line as a function of the depth in water along the Bragg peak for a single spot (σ_{xy} = 1 mm) of a 430 MeV/n carbon ion beam. The results of the modified MKM calculations based on the KC RDD (NIRS-QST model parameters) and the AMF (optimized model parameters) were radially integrated between 0 and 50 mm around the axis of the beam. (**B**–**E**) Comparison between the calculations using the modified MKM in conjunction with the KC RDD (NIRS-QST model parameters) and the AMF (optimized model parameters) as a function of the radial distance from the beam axis at four depths in water along the pristine peak (indicated by the black open squares in panel (**A**)). The vertical blue dashed lines demarcate voxels receiving at least 1% of the absorbed dose at the Bragg peak maximum.

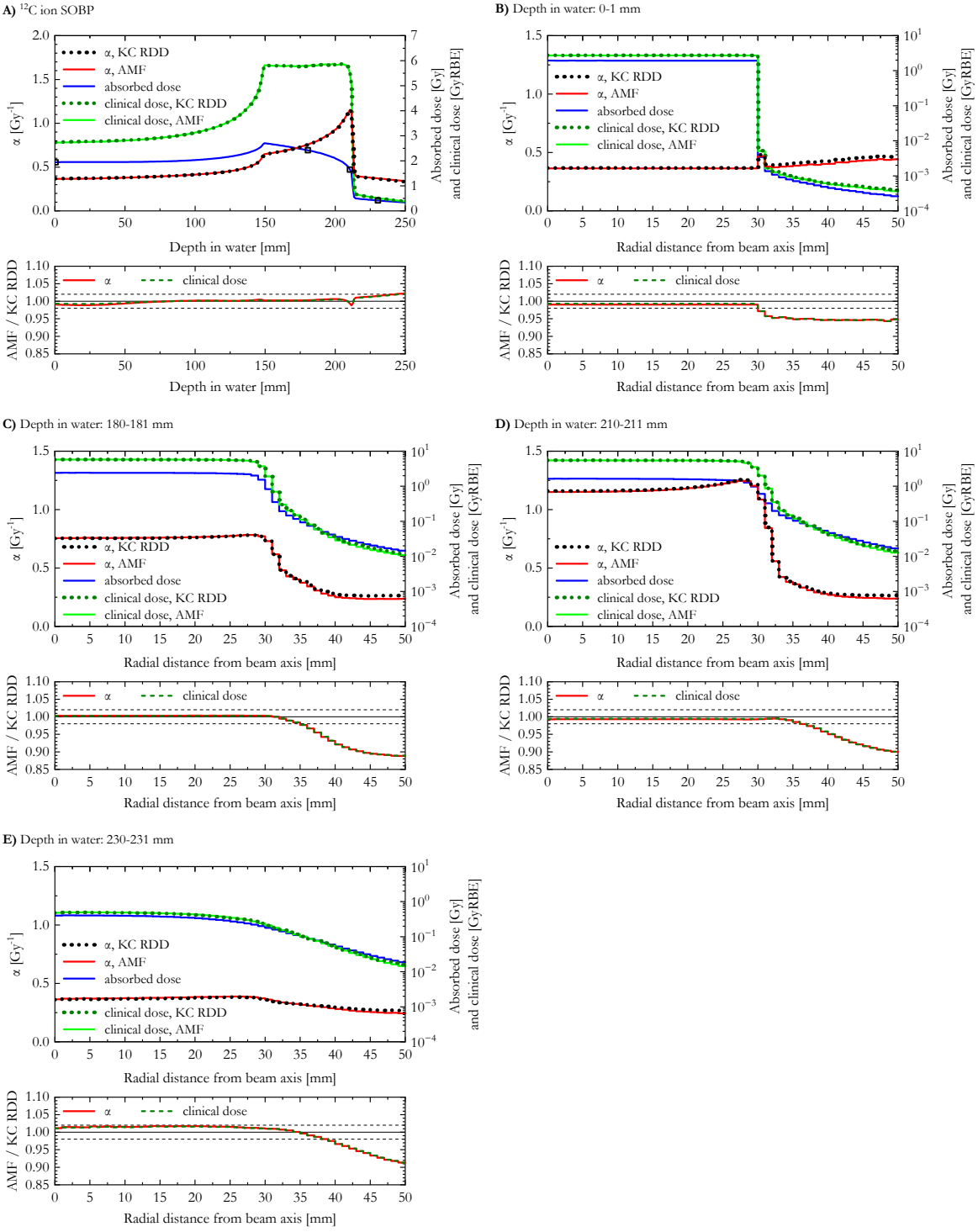


Figure 6. (**A**) α for the HSG cell line and the clinical dose as a function of the depth in water in the radially central part of a carbon ion SOBP with initial radius of 30 mm. The results of the modified MKM calculations based on the KC RDD (NIRS-QST model parameters) and the AMF (optimized model parameters) were radially integrated between 0 and 10 mm around the axis of the beam. (**B**–**E**) Comparison between the calculations using the modified MKM in conjunction with the KC RDD (NIRS-QST model parameters) and the AMF (optimized model parameters) as a function of the radial distance from the beam axis at four depths in water along the pristine peak (indicated by the black open squares in panel (**A**)).

4. Discussion

Descriptions of the radiation quality based on the radial dose distribution (RDD) around the particle path around matter are inherently limited by difficulties in the experimental assessment of such a physical quantity. By contrast, microdosimetric probability distributions can be readily assessed with specialized detectors, making them ideal candidates for quality assurance in external ion radiotherapy [98–100] and boron neutron capture therapy [101]. Since the parameters of RBE models are not interchangeable between approaches based on the RDD and those using microdosimetric distributions, modification of these parameters might be required to maintain consistency between the two methods [102].

The biological and clinical calculations for carbon ion radiotherapy at NIRS-QST [24] rely on the modified microdosimetric kinetic model (MKM) [31] together with the Kiefer–Chatterjee (KC) RDD [45,46] for cylindrical water targets. The results of Figures 4–6 indicate that, by appropriately tuning the modified MKM parameters (Table 1), it is possible to successfully reproduce the NIRS-QST methodology for carbon ion radiotherapy using microdosimetric probability density distributions for spherical targets instead of the KC RDD for cylindrical water targets. Therefore, these model parameters can be readily implemented in Monte Carlo transport codes and treatment planning systems for carbon ion radiotherapy in combination with approaches based on full or abridged microdosimetric probability distributions [48]. In contrast, because relevant deviations were observed for energetic proton and helium ions (Figure 2), it is strongly advised not to use the proposed model parameters for calculations involving primary beams of these ions.

In the current study, the microdosimetric distributions were assessed with a recently improved analytical microdosimetric function (AMF) [62] for water spheres with a target radius of 0.3 µm. As the results of this AMF were found to agree well with the corresponding experimental spectra measured with gas detectors [62], the modified MKM parameters presented in this work could be directly used in combination with such microdosimeters. It is important to note that, although the equivalent target radius of gas detectors is typically 0.5 µm [59] compared to 0.3 µm of our simulations, a previous study indicates that the RBE computed using spheres of these dimensions shows negligible differences [50]. On the other hand, further tuning of the modified MKM parameters may be necessary when applied to microdosimetric distributions obtained with solid-state detectors characterized by a larger sensitive volume [98].

Furthermore, although the comparison between AMF- and KC RDD- based calculations with the modified MKM included ^{20}Ne ions, the latter model is known to have limitations in reproducing the in vitro data for such heavy ions. Therefore, this comparison is intended solely to explore the potential differences between the KC RDD and the AMF. To address the limitations of the modified MKM at high LET and high doses, the stochastic MKM (SMKM) was proposed [57] and recently adapted at NIRS-QST for RBE calculations in hypofractionated and multi-ion radiotherapy with He, C, O, and Ne ions [103]. Since the SMKM at NIRS-QST is also based on KC RDD calculations, future work could build on the approach presented in this article to determine the SMKM model parameters suitable for use with simulated and experimentally measured microdosimetric distributions. Finally, it may be possible to approximate the results of a chosen RBE model, at least within a limited range of LET and ion types, by using another model with appropriately tuned model parameters.

5. Conclusions

The clinical dose calculations for carbon ion radiotherapy at NIRS-QST are based on the modified MKM in conjunction with the KC RDD. This study suggests that it is

possible to successfully reproduce these calculations using the AMF instead of the KC RDD, combined with the model parameters listed in Table 1.

Author Contributions: Software: A.P. and S.H.; formal analysis and visualization: A.P.; writing original draft: A.P.; manuscript review: all authors; funding acquisition and supervision: K.M.F. and C.J.B. All authors have read and agreed to the published version of the manuscript.

Funding: This research received no external funding.

Institutional Review Board Statement: Not applicable.

Informed Consent Statement: Not applicable.

Data Availability Statement: The data presented in this study are available on request from the corresponding author.

Conflicts of Interest: The authors declare no conflicts of interest.

Abbreviations

α	linear term of the linear quadratic model of cell survival
α_0	linear term of the linear quadratic model of cell survival for very sparsely radiation
AMF	analytical microdosimetric function
β	quadratic term of the linear quadratic model of cell survival
β_0	radiation-independent quadratic term of the linear quadratic model of cell survival
$D_{10\%}$	absorbed dose required to achieve a 10% surviving fraction
HSG cell line	human salivary gland tumor cells
KC RDD	Kiefer–Chatterjee radial dose distribution
LEM	local effect model
LET	linear energy transfer
LQM	linear quadratic model
MBM	mixed beam model
MKM	microdosimetric kinetic model
NIRS-QST	National Institute of Radiological Sciences within the National Institutes for Quantum Science and Technology
PHITS	Particle and Heavy Ion Transport code System
RBE	relative biological effectiveness
r_d	radius of the subnuclear domains
RDD	radial dose distribution
R_n	radius of the cell nucleus
SMKM	stochastic microdosimetric kinetic model
SOBP	spread-out Bragg peak
$\overline{z}_D^*$	saturation-corrected dose-mean specific energy

References

1. Durante, M.; Paganetti, H. Nuclear physics in particle therapy: A review. *Rep. Prog. Phys.* **2016**, *79*, 096702. [CrossRef] [PubMed]
2. Malouff, T.D.; Mahajan, A.; Krishnan, S.; Beltran, C.; Seneviratne, D.S.; Trifiletti, D.M. Carbon Ion Therapy: A Modern Review of an Emerging Technology. *Front. Oncol.* **2020**, *10*, 82. [CrossRef]
3. Paganetti, H.; Beltran, C.J.; Both, S.; Dong, L.; Flanz, J.B.; Furutani, K.M.; Grassberger, C.; Grosshans, D.R.; Knopf, A.-C.; A Langendijk, J.; et al. Roadmap: Proton therapy physics and biology. *Phys. Med. Biol.* **2021**, *66*, 05RM01. [CrossRef] [PubMed]
4. Inaniwa, T.; Kanematsu, N.; Noda, K.; Kamada, T. Treatment planning of intensity modulated composite particle therapy with dose and linear energy transfer optimization. *Phys. Med. Biol.* **2017**, *62*, 5180–5197. [CrossRef]
5. Kopp, B.; Mein, S.; Dokic, I.; Harrabi, S.; Böhlen, T.T.; Haberer, T.; Debus, J.; Abdollahi, A.; Mairani, A. Development and Validation of Single Field Multi-Ion Particle Therapy Treatments. *Int. J. Radiat. Oncol. Biol. Phys.* **2020**, *106*, 194–205. [CrossRef] [PubMed]

6. Mairani, A.; Mein, S.; Blakely, E.; Debus, J.; Durante, M.; Ferrari, A.; Fuchs, H.; Georg, D.; Grosshans, D.R.; Guan, F.; et al. Roadmap: Helium ion therapy. *Phys. Med. Biol.* **2022**, *67*, 15TR02. [CrossRef]
7. Scholz, M. Effects of Ion Radiation on Cells and Tissues. In *Radiation Effects on Polymers for Biological Use*; Springer: Berlin/Heidelberg, Germany, 2003; Volume 162, pp. 95–155.
8. Paganetti, H. Relative biological effectiveness (RBE) values for proton beam therapy. Variations as a function of biological endpoint, dose, and linear energy transfer. *Phys. Med. Biol.* **2014**, *59*, R419–R472. [CrossRef] [PubMed]
9. Tinganelli, W.; Durante, M. Carbon Ion Radiobiology. *Cancers* **2020**, *12*, 3022. [CrossRef] [PubMed]
10. Durante, M.; Debus, J.; Loeffler, J.S. Physics and biomedical challenges of cancer therapy with accelerated heavy ions. *Nat. Rev. Phys.* **2021**, *3*, 777–790. [CrossRef]
11. IAEA. *TRS 461: Relative Biological Effectiveness in Ion Beam Therapy*; Technical Report Series; IAEA: Vienna, Austria, 2008.
12. Paganetti, H.; Niemierko, A.; Ancukiewicz, M.; E Gerweck, L.; Goitein, M.; Loeffler, J.S.; Suit, H.D. Relative biological effectiveness (RBE) values for proton beam therapy. *Int. J. Radiat. Oncol. Biol. Phys.* **2002**, *53*, 407–421. [CrossRef]
13. ICRU. Report 78: Prescribing, Recording and Reporting Proton-beam Therapy. *Radiat. Prot. Dosim.* **2009**, *133*, 60–62. [CrossRef]
14. Jones, B. Why RBE must be a variable and not a constant in proton therapy. *Br. J. Radiol.* **2016**, *89*, 20160116. [CrossRef] [PubMed]
15. Paganetti, H.; Blakely, E.; Carabe-Fernandez, A.; Carlson, D.J.; Das, I.J.; Dong, L.; Grosshans, D.; Held, K.D.; Mohan, R.; Moiseenko, V.; et al. Report of the AAPM TG-256 on the relative biological effectiveness of proton beams in radiation therapy. *Med. Phys.* **2019**, *46*, e53–e78. [CrossRef] [PubMed]
16. McMahon, S.J. Proton RBE models: Commonalities and differences. *Phys. Med. Biol.* **2021**, *66*, 04NT02. [CrossRef]
17. Sorensen, B.S.; Pawelke, J.; Bauer, J.; Burnet, N.; Dasu, A.; Høyer, M.; Karger, C.; Krause, M.; Schwarz, M.; Underwood, T.; et al. Does the uncertainty in relative biological effectiveness affect patient treatment in proton therapy? *Radiother. Oncol.* **2021**, *163*, 177–184. [CrossRef] [PubMed]
18. Parisi, A.; Beltran, C.J.; Furutani, K.M. Variable RBE in proton radiotherapy: A comparative study with the predictive Mayo Clinic Florida microdosimetric kinetic model and phenomenological models of cell survival. *Phys. Med. Biol.* **2023**, *68*, 185020. [CrossRef]
19. Paganetti, H.; Simone, C.B.; Bosch, W.R.; Haas-Kogan, D.; Kirsch, D.G.; Li, H.; Liang, X.; Liu, W.; Mahajan, A.; Story, M.D.; et al. NRG Oncology White Paper on the Relative Biological Effectiveness in Proton Therapy. *Int. J. Radiat. Oncol.* **2024**, *121*, 202–217. [CrossRef] [PubMed]
20. Kanai, T.; Endo, M.; Minohara, S.; Miyahara, N.; Koyama-Ito, H.; Tomura, H.; Matsufuji, N.; Futami, Y.; Fukumura, A.; Hiraoka, T.; et al. Biophysical characteristics of HIMAC clinical irradiation system for heavy-ion radiation therapy. *Int. J. Radiat. Oncol. Biol. Phys.* **1999**, *44*, 201–210. [CrossRef] [PubMed]
21. Jäkel, O.; Krämer, M.; Karger, C.P.; Debus, J. Treatment planning for heavy ion radiotherapy: Clinical implementation and application. *Phys. Med. Biol.* **2001**, *46*, 1101–1116. [CrossRef]
22. Kramer, M.; Scholz, M. Rapid calculation of biological effects in ion radiotherapy. *Phys. Med. Biol.* **2006**, *51*, 1959–1970. [CrossRef] [PubMed]
23. Inaniwa, T.; Furukawa, T.; Kase, Y.; Matsufuji, N.; Toshito, T.; Matsumoto, Y.; Furusawa, Y.; Noda, K. Treatment planning for a scanned carbon beam with a modified microdosimetric kinetic model. *Phys. Med. Biol.* **2010**, *55*, 6721–6737. [CrossRef] [PubMed]
24. Inaniwa, T.; Furukawa, T.; Kase, Y.; Matsufuji, N.; Toshito, T.; Matsumoto, Y.; Furusawa, Y.; Noda, K. Reformulation of a clinical-dose system for carbon-ion radiotherapy treatment planning at the National Institute of Radiological Sciences, Japan. *Phys. Med. Biol.* **2015**, *60*, 3271–3286. [CrossRef]
25. Karger, C.P.; Peschke, P. RBE and related modeling in carbon-ion therapy. *Phys. Med. Biol.* **2017**, *63*, 01TR02. [CrossRef] [PubMed]
26. Fossati, P.; Matsufuji, N.; Kamada, T.; Karger, C.P. Radiobiological issues in prospective carbon ion therapy trials. *Med. Phys.* **2018**, *45*, e1096–e1110. [CrossRef] [PubMed]
27. Mein, S.; Klein, C.; Kopp, B.; Magro, G.; Harrabi, S.; Karger, C.P.; Haberer, T.; Debus, J.; Abdollahi, A.; Dokic, I.; et al. Assessment of RBE-Weighted Dose Models for Carbon Ion Therapy Toward Modernization of Clinical Practice at HIT: In Vitro, In Vivo, and in Patients. *Int. J. Radiat. Oncol. Biol. Phys.* **2020**, *108*, 779–791. [CrossRef] [PubMed]
28. Fujitaka, S.; Fujii, Y.; Nihongi, H.; Nakayama, S.; Takashina, M.; Hamatani, N.; Tsubouchi, T.; Yagi, M.; Minami, K.; Ogawa, K.; et al. Physical and biological beam modeling for carbon beam scanning at Osaka Heavy Ion Therapy Center. *J. Appl. Clin. Med. Phys.* **2021**, *22*, 77–92. [CrossRef] [PubMed]
29. Scholz, M.; Kellerer, A.M.; Kraft-Weyrather, W.; Kraft, G. Computation of cell survival in heavy ion beams for therapy. The model and its approximation. *Radiat. Environ. Biophys.* **1997**, *36*, 59–66. [CrossRef]
30. Kanai, T.; Furusawa, Y.; Fukutsu, K.; Itsukaichi, H.; Eguchi-Kasai, K.; Ohara, H. Irradiation of mixed beam and design of spread-out Bragg peak for heavy-ion radiotherapy. *Radiat. Res.* **1997**, *147*, 78–85. [CrossRef]
31. Kase, Y.; Kanai, T.; Matsumoto, Y.; Furusawa, Y.; Okamoto, H.; Asaba, T.; Sakama, M.; Shinoda, H. Microdosimetric measurements and estimation of human cell survival for heavy-ion beams. *Radiat. Res.* **2006**, *166*, 629–638. [CrossRef] [PubMed]

32. Elsässer, T.; Scholz, M. Cluster effects within the local effect model. *Radiat. Res.* **2007**, *167*, 319–329. [CrossRef]
33. Elsässer, T.; Krämer, M.; Scholz, M. Accuracy of the local effect model for the prediction of biologic effects of carbon ion beams in vitro and in vivo. *Int. J. Radiat. Oncol. Biol. Phys.* **2008**, *71*, 866–872. [CrossRef]
34. Elsasser, T.; Weyrather, W.K.; Friedrich, T.; Durante, M.; Iancu, G.; Krämer, M.; Kragl, G.; Brons, S.; Winter, M.; Weber, K.; et al. Quantification of the relative biological effectiveness for ion beam radiotherapy: Direct experimental comparison of proton and carbon ion beams and a novel approach for treatment planning. *Int. J. Radiat. Oncol. Biol. Phys.* **2010**, *78*, 1177–1183. [CrossRef]
35. Bellinzona, V.E.; Cordoni, F.; Missiaggia, M.; Tommasino, F.; Scifoni, E.; La Tessa, C.; Attili, A. Linking Microdosimetric Measurements to Biological Effectiveness in Ion Beam Therapy: A Review of Theoretical Aspects of MKM and Other Models. *Front. Phys.* **2021**, *8*, 578492. [CrossRef]
36. Parisi, A.; Furutani, K.M.; Beltran, C.J. On the calculation of the relative biological effectiveness of ion radiation therapy using a biological weighting function, the microdosimetric kinetic model (MKM) and subsequent corrections (non-Poisson MKM and modified MKM). *Phys. Med. Biol.* **2022**, *67*, 095014. [CrossRef] [PubMed]
37. Colautti, P.; Conte, V.; Selva, A.; Chiriotti, S.; Pola, A.; Bortot, D.; Fazzi, A.; Agosteo, S.; Treccani, M.; Nardo, L.; et al. Miniaturized microdosimeters as LET monitors: First comparison of calculated and experimental data performed at the 62 MeV/u (12)C beam of INFN-LNS with four different detectors. *Phys. Med.* **2018**, *52*, 113–121. [CrossRef] [PubMed]
38. Magrin, G. A method to convert spectra from slab microdosimeters in therapeutic ion-beams to the spectra referring to microdosimeters of different shapes and material. *Phys. Med. Biol.* **2018**, *63*, 215021. [CrossRef] [PubMed]
39. Villagrasa, C.; Bordage, M.C.; Bueno, M.; Bug, M.; Chiriotti, S.; Gargioni, E.; Heide, B.; Nettelbeck, H.; Parisi, A.; Rabus, H. Assessing the Contribution of Cross-Sections to the Uncertainty of Monte Carlo Calculations in Micro- and Nanodosimetry. *Radiat. Prot. Dosim.* **2019**, *183*, 11–16. [CrossRef] [PubMed]
40. Conte, V.; Agosteo, S.; Bianchi, A.; Bolst, D.; Bortot, D.; Catalano, R.; Cirrone, G.A.P.; Colautti, P.; Cuttone, G.; Guatelli, S.; et al. Microdosimetry of a therapeutic proton beam with a mini-TEPC and a MicroPlus-Bridge detector for RBE assessment. *Phys. Med. Biol.* **2020**, *65*, 245018. [CrossRef]
41. Parisi, A.; Olko, P.; Swakoń, J.; Horwacik, T.; Jabłoński, H.; Malinowski, L.; Nowak, T.; Struelens, L.; Vanhavere, F. Microdosimetric characterization of a clinical proton therapy beam: Comparison between simulated lineal energy distributions in spherical water targets and experimental measurements with a silicon detector. *Phys. Med. Biol.* **2022**, *67*, 015006. [CrossRef] [PubMed]
42. Parisi, A.; Beltran, C.J.; Furutani, K.M. The Mayo Clinic Florida microdosimetric kinetic model of clonogenic survival: Formalism and first benchmark against in vitro and in silico data. *Phys. Med. Biol.* **2022**, *67*, 185013. [CrossRef] [PubMed]
43. Bianchi, A.; Selva, A.; Colautti, P.; Bortot, D.; Mazzucconi, D.; Pola, A.; Agosteo, S.; Petringa, G.; Cirrone, G.; Reniers, B.; et al. Microdosimetry with a sealed mini-TEPC and a silicon telescope at a clinical proton SOBP of CATANA. *Radiat. Phys. Chem.* **2020**, *171*, 108730. [CrossRef]
44. Hartzell, S. Impact of microdosimetric modelling on the computation of relative biological effectiveness for carbon ion radiation therapy. 2024; *submitted for publication*.
45. Chatterjee, A.; Schaefer, H.J. Microdosimetric structure of heavy ion tracks in tissue. *Radiat. Environ. Biophys.* **1976**, *13*, 215–227. [CrossRef] [PubMed]
46. Kiefer, J.; Straaten, H. A model of ion track structure based on classical collision dynamics. *Phys. Med. Biol.* **1986**, *31*, 1201–1209. [CrossRef]
47. Beltran, C.; Amos, R.A.; Rong, Y. We are ready for clinical implementation of Carbon Ion Radiotherapy in the United States. *J. Appl. Clin. Med. Phys.* **2020**, *21*, 6–9. [CrossRef] [PubMed]
48. Parisi, A.; Beltran, C.J.; Furutani, K.M. A methodology to abridge microdosimetric distributions without a significant loss of the spectral information needed for the RBE computation in carbon ion therapy. *J. Appl. Clin. Med. Phys.* **2023**, *24*, e14049. [CrossRef] [PubMed]
49. Sato, T.; Iwamoto, Y.; Hashimoto, S.; Ogawa, T.; Furuta, T.; Abe, S.-I.; Kai, T.; Matsuya, Y.; Matsuda, N.; Hirata, Y.; et al. Recent improvements of the particle and heavy ion transport code system—PHITS version 3.33. *J. Nucl. Sci. Technol.* **2023**, *61*, 127–135. [CrossRef]
50. Parisi, A.; Furutani, K.M.; Sato, T.; Beltran, C.J. Comparative Evaluation of Two Analytical Functions for the Microdosimetry of Ions from ^{1}H to ^{238}U. *Quantum Beam Sci.* **2024**, *8*, 18. [CrossRef]
51. Fowler, J.F. The linear-quadratic formula and progress in fractionated radiotherapy. *Br. J. Radiol.* **1989**, *62*, 679–694. [CrossRef] [PubMed]
52. McMahon, S.J. The linear quadratic model: Usage, interpretation and challenges. *Phys. Med. Biol.* **2018**, *64*, 01TR01. [CrossRef] [PubMed]
53. Hawkins, R.B. A statistical theory of cell killing by radiation of varying linear energy transfer. *Radiat. Res.* **1994**, *140*, 366–374. [CrossRef]

54. Kellerer, A.M.; Rossi, H.D. The theory of dual radiation action. *Curr. Top. Radiat. Res. Quart.* **1972**, *8*, 85–158.
55. Kellerer, A.M.; Rossi, H.H. A generalized formulation of dual radiation action. *Radiat. Res.* **1978**, *75*, 471–488. [CrossRef]
56. Hawkins, R.B. A microdosimetric-kinetic model for the effect of non-Poisson distribution of lethal lesions on the variation of RBE with LET. *Radiat. Res.* **2003**, *160*, 61–69. [CrossRef] [PubMed]
57. Sato, T.; Furusawa, Y. Cell survival fraction estimation based on the probability densities of domain and cell nucleus specific energies using improved microdosimetric kinetic models. *Radiat. Res.* **2012**, *178*, 341–356. [CrossRef] [PubMed]
58. ICRU. ICRU Report 85: Fundamental Quantities and Units for Ionizing Radiation. *J. ICRU* **2011**, *11*, 1–31.
59. ICRU. ICRU Report 98: Stochastic Nature of Radiation Interactions: Microdosimetry. *J. ICRU* **2023**, *23*, 1–168. [CrossRef]
60. Kase, Y.; Matsufuji, N.; Elsässer, T.; Kanai, T.; Furusawa, Y.; Scholz, M. Biophysical calculation of cell survival probabilities using amorphous track structure models for heavy-ion irradiation. *Phys. Med. Biol.* **2008**, *53*, 37–59. [CrossRef]
61. Sato, T.; Watanabe, R.; Niita, K. Development of a calculation method for estimating specific energy distribution in complex radiation fields. *Radiat. Prot. Dosim.* **2006**, *122*, 41–45. [CrossRef]
62. Sato, T.; Matsuya, Y.; Ogawa, T.; Kai, T.; Hirata, Y.; Tsuda, S.; Parisi, A. Improvement of the hybrid approach between Monte Carlo simulation and analytical function for calculating microdosimetric probability densities in macroscopic matter. *Phys. Med. Biol.* **2023**, *68*, 155005. [CrossRef]
63. Butts, J.J.; Katz, R. Theory of RBE for heavy ion bombardment of dry enzymes and viruses. *Radiat. Res.* **1967**, *30*, 855–871. [CrossRef] [PubMed]
64. Tomita, H.; Kai, M.; Kusama, T.; Ito, A. Monte Carlo simulation of physicochemical processes of liquid water radiolysis. The effects of dissolved oxygen and OH scavenger. *Radiat. Environ. Biophys.* **1997**, *36*, 105–116. [CrossRef] [PubMed]
65. Olko, P.; Booz, J. Energy deposition by protons and alpha particles in spherical sites of nanometer to micrometer diameter. *Radiat. Environ. Biophys.* **1990**, *29*, 1–17. [CrossRef]
66. Tsuda, S.; Sato, T.; Takahashi, F.; Satoh, D.; Sasaki, S.; Namito, Y.; Iwase, H.; Ban, S.; Takada, M. Systematic measurement of lineal energy distributions for proton, He and Si ion beams over a wide energy range using a wall-less tissue equivalent proportional counter. *J. Radiat. Res.* **2012**, *53*, 264–271. [CrossRef] [PubMed]
67. Takada, K.; Sato, T.; Kumada, H.; Koketsu, J.; Takei, H.; Sakurai, H.; Sakae, T. Validation of the physical and RBE-weighted dose estimator based on PHITS coupled with a microdosimetric kinetic model for proton therapy. *J. Radiat. Res.* **2018**, *59*, 91–99. [CrossRef] [PubMed]
68. Tsuda, S.; Sato, T.; Takahashi, F.; Satoh, D.; Endo, A.; Sasaki, S.; Namito, Y.; Iwase, H.; Ban, S.; Takada, M. Measurement of microdosimetric spectra with a wall-less tissue-equivalent proportional counter for a 290 MeV/u 12C beam. *Phys. Med. Biol.* **2010**, *55*, 5089–5101. [CrossRef]
69. Hu, N.; Tanaka, H.; Takata, T.; Endo, S.; Masunaga, S.; Suzuki, M.; Sakurai, Y. Evaluation of PHITS for microdosimetry in BNCT to support radiobiological research. *Appl. Radiat. Isot.* **2020**, *161*, 109148. [CrossRef] [PubMed]
70. Parisi, A.; Hoey, O.A.; Mégret, P.; Vanhavere, F. Microdosimetric specific energy probability distribution in nanometric targets and its correlation with the efficiency of thermoluminescent detectors exposed to charged particles. *Radiat. Meas.* **2019**, *123*, 1–12. [CrossRef]
71. Matsuya, Y.; Sasaki, K.; Yoshii, Y.; Okuyama, G.; Date, H. Integrated Modelling of Cell Responses after Irradiation for DNA-Targeted Effects and Non-Targeted Effects. *Sci. Rep.* **2018**, *8*, 4849. [CrossRef]
72. Parisi, A.; Sato, T.; Matsuya, Y.; Kase, Y.; Magrin, G.; Verona, C.; Tran, L.; Rosenfeld, A.; Bianchi, A.; Olko, P.; et al. Development of a new microdosimetric biological weighting function for the RBE_{10} assessment in case of the V79 cell line exposed to ions from ^{1}H to ^{238}U. *Phys. Med. Biol.* **2020**, *65*, 235010. [CrossRef]
73. Sato, T.; Watanabe, R.; Kase, Y.; Tsuruoka, C.; Suzuki, M.; Furusawa, Y.; Niita, K. Analysis of cell-survival fractions for heavy-ion irradiations based on microdosimetric kinetic model implemented in the particle and heavy ion transport code system. *Radiat. Prot. Dosim.* **2011**, *143*, 491–496. [CrossRef] [PubMed]
74. Matsuya, Y.; Fukunaga, H.; Omura, M.; Date, H. A Model for Estimating Dose-Rate Effects on Cell-Killing of Human Melanoma after Boron Neutron Capture Therapy. *Cells* **2020**, *9*, 1117. [CrossRef] [PubMed]
75. Parisi, A.; Struelens, L.; Vanhavere, F. Comparison between the results of a recently-developed biological weighting function (V79-RBE_{10}BWF) and thein vitroclonogenic survival RBE_{10} of other repair-competent asynchronized normoxic mammalian cell lines and ions not used for the development of the model. *Phys. Med. Biol.* **2021**, *66*, 235006.
76. Sato, T.; Hashimoto, S.; Inaniwa, T.; Takada, K.; Kumada, H. Implementation of simplified stochastic microdosimetric kinetic models into PHITS for application to radiation treatment planning. *Int. J. Radiat. Biol.* **2021**, *97*, 1450–1460. [CrossRef]
77. Parisi, A.; Beltran, C.J.; Furutani, K.M. The Mayo Clinic Florida Microdosimetric Kinetic Model of Clonogenic Survival: Application to Various Repair-Competent Rodent and Human Cell Lines. *Int. J. Mol. Sci.* **2022**, *23*, 12491. [CrossRef] [PubMed]
78. Parisi, A.; Furutani, K.M.; Sato, T.; Beltran, C.J. LET-based approximation of the microdosimetric kinetic model for proton radiotherapy. *Med. Phys.* **2024**, *51*, 7589–7605. [CrossRef] [PubMed]

79. Parisi, A.; Dabin, J.; Schoonjans, W.; Van Hoey, O.; Mégret, P.; Vanhavere, F. Photon energy response of LiF:Mg,Ti (MTS) and LiF:Mg,Cu,P (MCP) thermoluminescent detectors: Experimental measurements and microdosimetric modeling. *Radiat. Phys. Chem.* **2019**, *163*, 67–73. [CrossRef]
80. Parisi, A.; Struelens, L.; Vanhavere, F. Nanoscale calculation of the relative efficiency of 7LiF:Mg,Ti (MTS-7) and 7LiF:Mg,Cu,P (MCP-7) thermoluminescent detectors for measuring electrons and positrons. *J. Phys. Conf. Ser.* **2020**, *1662*, 012025. [CrossRef]
81. Parisi, A.; Olko, P.; Swakoń, J.; Horwacik, T.; Jabłoński, H.; Malinowski, L.; Nowak, T.; Struelens, L.; Vanhavere, F. Modeling the radiation-induced cell death in a therapeutic proton beam using thermoluminescent detectors and radiation transport simulations. *Phys. Med. Biol.* **2020**, *65*, 015008. [CrossRef] [PubMed]
82. Parisi, A.; Struelens, L.; Vanhavere, F. The relative efficiency of ^{7}LiF:Mg,Ti (MTS-7) and ^{7}LiF:Mg,Cu,P (MCP-7) thermoluminescent detectors for muons, pions and kaons over a broad energy range (2 keV–1 GeV): Theoretical calculations using the Microdosimetric d(z) Model. *Radiat. Phys. Chem.* **2020**, *177*, 109096. [CrossRef]
83. Parisi, A.; Olko, P.; Swakoń, J.; Horwacik, T.; Jabłoński, H.; Malinowski, L.; Nowak, T.; Struelens, L.; Vanhavere, F. A new method to predict the response of thermoluminescent detectors exposed at different positions within a clinical proton beam. *Radiat. Meas.* **2020**, *133*, 106281. [CrossRef]
84. Hirata, Y.; Sato, T.; Watanabe, K.; Ogawa, T.; Parisi, A.; Uritani, A. Theoretical and experimental estimation of the relative optically stimulated luminescence efficiency of an optical-fiber-based BaFBr:Eu detector for swift ions. *J. Nucl. Sci. Technol.* **2022**, *59*, 915–924. [CrossRef]
85. Parisi, A.; Sawakuchi, G.; Granville, D.; Yukihara, E.G. Microdosimetric modeling of the relative efficiency of Al_2O_3:C (Luxel, blue emission) optically stimulated luminescent detectors exposed to ions from ^{1}H to ^{132}Xe. *Radiat. Meas.* **2022**, *150*, 106678. [CrossRef]
86. Sato, T.; Matsuya, Y.; Hamada, N. Microdosimetric Modeling of Relative Biological Effectiveness for Skin Reactions: Possible Linkage Between In Vitro and In Vivo Data. *Int. J. Radiat. Oncol. Biol. Phys.* **2022**, *114*, 153–162. [CrossRef]
87. Furusawa, Y.; Fukutsu, K.; Aoki, M.; Itsukaichi, H.; Eguchi-Kasai, K.; Ohara, H.; Yatagai, F.; Kanai, T.; Ando, K. Inactivation of Aerobic and Hypoxic Cells from Three Different Cell Lines by Accelerated3He-,12C- and20Ne-Ion Beams. *Radiat. Res.* **2000**, *154*, 485–496. [CrossRef]
88. Hirayama, H.; Namito, Y.; Bielajew, A.F.; Wilderman, S.J.; Nelson, W.R. *SLAC-R-730 The EGS5 Code System*; Stanford Linear Accelerator Center: Menlo Park, CA, USA, 2005.
89. Vavilov, P.V. Ionization Losses of High-Energy Heavy Particles. *Soviet Phys. JETP* **1957**, *5*, 749–751.
90. Lynch, G.R.; Dahl, O.I. Approximations to multiple Coulomb scattering. *Nucl. Instrum. Methods Phys. Res. Sect. B Beam Interact. Mater. At.* **1991**, *58*, 6–10. [CrossRef]
91. Niita, K.; Chiba, S.; Maruyama, T.; Maruyama, T.; Takada, H.; Fukahori, T.; Nakahara, Y.; Iwamoto, A. Analysis of the (N,xN′) reactions by quantum molecular dynamics plus statistical decay model. *Phys. Rev. C Nucl. Phys.* **1995**, *52*, 2620–2635. [CrossRef]
92. Boudard, A.; Cugnon, J.; David, J.-C.; Leray, S.; Mancusi, D. New potentialities of the Liège intranuclear cascade model for reactions induced by nucleons and light charged particles. *Phys. Rev. C* **2013**, *87*, 014606. [CrossRef]
93. Furihata, S. Statistical analysis of light fragment production from medium energy proton-induced reactions. *Nucl. Instrum. Methods Phys. Res. Sect. B-Beam Interact. Mater. At.* **2000**, *171*, 251–258. [CrossRef]
94. Iwamoto, Y.; Niita, K.; Sato, T.; Matsuda, N.; Iwase, H.; Nakashima, H.; Sakamoto, Y. Validation of the event generator mode in the PHITS code and its application. In Proceedings of the International Conference on Nuclear Data for Science and Technology 2007 (Nd2007), Nice, France, 22–27 April 2007; EDP Sciences: Les Ulis, France, 2008.
95. Ogawa, T.; Sato, T.; Hashimoto, S.; Niita, K. Development of a reaction ejectile sampling algorithm to recover kinematic correlations from inclusive cross-section data in Monte-Carlo particle transport simulations. *Nucl. Instrum. Methods Phys. Res. Sect. A Accel. Spectrometers Detect. Assoc. Equip.* **2014**, *763*, 575–590. [CrossRef]
96. ICRU. *ICRU Report 90: Key Data For Ionizing-Radiation Dosimetry*; Oxford University Press: Bethesda, MD, USA, 2016.
97. Parisi, A.; Furutani, K.M.; Beltran, C.J. Variation of the relative biological effectiveness in the penumbra of ion therapy beams estimated using different microdosimetric approaches. *Phys. Imaging Radiat. Oncol.* **2024**, *29*, 100564. [CrossRef]
98. Tran, L.T.; Bolst, D.; James, B.; Pan, V.; Vohradsky, J.; Peracchi, S.; Chartier, L.; Debrot, E.; Guatelli, S.; Petasecca, M.; et al. Silicon 3D Microdosimeters for Advanced Quality Assurance in Particle Therapy. *Appl. Sci.* **2021**, *12*, 328. [CrossRef]
99. Bianchi, A.; Selva, A.; Colautti, P.; Petringa, G.; Cirrone, P.; Reniers, B.; Parisi, A.; Vanhavere, F.; Conte, V. Repeatability and Reproducibility of Microdosimetry With a Mini-TEPC. *Front. Phys.* **2021**, *9*, 727816. [CrossRef]
100. Magrin, G.; Palmans, H.; Stock, M.; Georg, D. State-of-the-art and potential of experimental microdosimetry in ion-beam therapy. *Radiother. Oncol.* **2023**, *182*, 109586. [CrossRef]
101. Kumada, H.; Masuda, A.; Tanaka, H.; Takada, M.; Hu, N. New technologies for beam spectrometry, quality assurance, real-time monitoring and microdosimetry in BNCT. *Radiat. Meas.* **2024**, *177*, 107276. [CrossRef]

102. Lee, S.H.; Mizushima, K.; Yonai, S.; Matsumoto, S.; Mizuno, H.; Nakaji, T.; Kohno, R.; Iwata, Y.; Shirai, T.; Pan, V.; et al. Predicting the Biological Effects of Human Salivary Gland Tumour Cells for Scanned 4He-, 12C-, 16O-, and 20Ne-Ion Beams Using an SOI Microdosimeter. *Appl. Sci.* **2022**, *12*, 6148. [CrossRef]
103. Inaniwa, T.; Kanematsu, N. Adaptation of stochastic microdosimetric kinetic model for charged-particle therapy treatment planning. *Phys. Med. Biol.* **2018**, *63*, 095011. [CrossRef] [PubMed]

Disclaimer/Publisher's Note: The statements, opinions and data contained in all publications are solely those of the individual author(s) and contributor(s) and not of MDPI and/or the editor(s). MDPI and/or the editor(s) disclaim responsibility for any injury to people or property resulting from any ideas, methods, instructions or products referred to in the content.